Journal of
**Applied**
**Crystallography**

ISSN 0021-8898

Editor: **Anke R. Kaysser-Pyzalla**

# Three-dimensional X-ray diffraction imaging of process-induced dislocation loops in silicon

**David Allen, Jochen Wittge, Jennifer Stopford, Andreas Danilewsky and Patrick McNally**

*J. Appl. Cryst.* (2011). **44**, 526–531

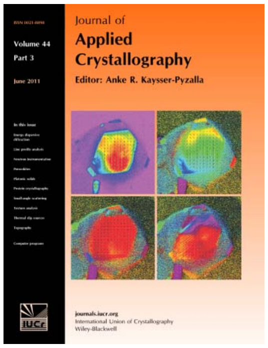

Journal of
Applied
Crystallography
ISSN 0021-8898

Received 5 August 2010
Accepted 8 April 2011

# Three-dimensional X-ray diffraction imaging of process-induced dislocation loops in silicon

David Allen,[a]* Jochen Wittge,[b] Jennifer Stopford,[a] Andreas Danilewsky[b] and Patrick McNally[a]

[a]The Rince Institute, Dublin City University, Dublin 9, Ireland, and [b]Kristallographie, Institut für Geowissenschaften, Albert-Ludwigs Universität, Freiburg, Germany. Correspondence e-mail: david.allen2@mail.dcu.ie

In the semiconductor industry, wafer handling introduces micro-cracks at the wafer edge and the causal relationship of these cracks to wafer breakage is a difficult task. By way of understanding the wafer breakage process, a series of nano-indents were introduced both into $20 \times 20$ mm (100) wafer pieces and into whole wafers as a means of introducing controlled strain. Visualization of the three-dimensional structure of crystal defects has been demonstrated. The silicon samples were then treated by various thermal anneal processes to initiate the formation of dislocation loops around the indents. This article reports the three-dimensional X-ray diffraction imaging and visualization of the structure of these dislocations. A series of X-ray section topographs of both the indents and the dislocation loops were taken at the ANKA Synchrotron, Karlsruhe, Germany. The topographs were recorded on a CCD system combined with a high-resolution scintillator crystal and were measured by repeated cycles of exposure and sample translation along a direction perpendicular to the beam. The resulting images were then rendered into three dimensions utilizing open-source three-dimensional medical tomography algorithms that show the dislocation loops formed. Furthermore this technique allows for the production of a video (avi) file showing the rotation of the rendered topographs around any defined axis. The software also has the capability of splitting the image along a segmentation line and viewing the internal structure of the strain fields.

## 1. Introduction

White-beam synchrotron X-ray topography is a widely used nondestructive characterization technique for the visualization of defects and the characterization of both long-range and short-range strain in crystals (Authier *et al.*, 1996; Danilewsky *et al.*, 2003, 2008; Authier, 2004)

The most widely used technique for the study of crystal characteristics is transmission topography in the Laue condition in both large-area and section transmission (Guinier & Tennevin, 1949; Kawado *et al.*, 2005; Lang, 1959*a*,*b*). This technique was later expanded with the use of synchrotron radiation to obtain high-resolution topographs by Tuomi *et al.* (1974) and Hart (1975).

Early three-dimensional characterization techniques involved the use of stereo topographs recorded as a pair in the $hkl$ and $\overline{hkl}$ reflections (Lang, 1959*b*) or the use of step-scanning section topography (Kawado & Aoyama, 1979), the latter technique requiring the use of an automatic Bragg angle corrector. Later techniques evolved into combined topography and tomography (Ludwig *et al.*, 2001; Kawado *et al.*, 2004, 2005, and references therein), an approach that consisted of recording a series of images while rotating the sample around its diffraction vector. The application of imaging software to combine the section topographs has also been employed, freeing the researcher from the tedious pen and pencil approach used previously (Mukaide *et al.*, 2006).

More recently, Kvardakov *et al.* (2007) demonstrated the ability to observe the defect distribution in a crystal utilizing section transmission topography and image processing software. This technique also avoids the troublesome use of tomography where the crystal orientation of the sample must be adjusted precisely to the rotation of the goniometer (Kajiwara *et al.*, 2007).

The present paper describes a three-dimensional X-ray diffraction imaging (3D-XRDI) technique, utilizing section transmission (ST) topography, that allows for the production of three-dimensional images but does not involve rotation of the sample around the diffraction vector, instead simply using vertical translation of the sample through the incident beam combined with available imaging software. The technique is similar to that used by Kvardakov *et al.* (2007) but with the acquisition time for each topograph reduced to $<500$ ms.

## 2. Experimental method

Defined defects were introduced into crystalline silicon with (100) surface crystallographic orientation, for both whole

doi:10.1107/S0021889811013264

200 mm-diameter wafers and silicon samples approximately 20 × 20 mm in size, using a Nano-indenter II equipped with a sharp Berkovich tip to give indentation forces of 100–600 mN or a sharp Vickers tip to give indentation forces of 2–20 N. Both the wafers and the wafer pieces underwent a plateau anneal to 1273 K for a period of 120 s (Danilewsky *et al.*, 2010) in order to produce dislocation loops. The sample was annealed using a double ellipsoid mirror heater with the sample held at the common focal point of the two heating lamps. The heater has a maximum vertical temperature gradient of 18 K $\mathrm{cm}^{-1}$ and a maximum horizontal temperature gradient of 8 K $\mathrm{cm}^{-1}$. The wafers were annealed using a Jiplelec JetFirst 200C thermal anneal system and underwent a plateau anneal to 1273 K for 60 s.

Post thermal anneal, the samples were analysed by X-ray diffraction imaging at the synchrotron light source ANKA, Institute for Synchrotron Radiation, Karlsruhe Institute of Technology, Germany. The experiments were carried out at the Topo-Tomo beamline using a white X-ray beam sourced from a 1.5 T bending magnet and fed by a 2.5 GeV storage ring (Cholewa & Rack, 2007). The beamline is 30 m in length with a single optical component, a 0.5 mm-thick polished beryllium window positioned directly in front of the experiment; a set of slits is positioned 4.8 m from the source point, which allows for good pre-definition of the beam, a reduction of the heat load on subsequent components and control over beam divergence. A second set of tungsten slits are positioned 28 m from the source, which are utilized to collimate the beam to 10 × 1 mm (Danilewsky *et al.*, 2003, 2008; Rack *et al.*, 2009; Simon & Danilewsky, 2003).

The incident beam was then collimated to 10 mm × 15 μm in size by a final vacuum slit system positioned 30 cm from the sample. Fig. 1 shows the setup for the experimental procedure; it can be seen that the incident beam is diffracted at different depths within the sample (only the two external surfaces are shown in the schematic), so providing direct depth information for defects within the sample (McNally *et al.*, 2001; Tanner, 1989). Fig. 2 shows the setup utilized to capture the ST topographs. The sample holder was mounted on a goniometer capable of $x$–$z$ translation movement and $\varphi$ swivel movement. Utilizing the $\varphi$ translation the sample was tilted to 12° to capture the $2\bar{2}0$ reflection (Danilewsky *et al.*, 2008; Tuomi *et al.*, 1974).

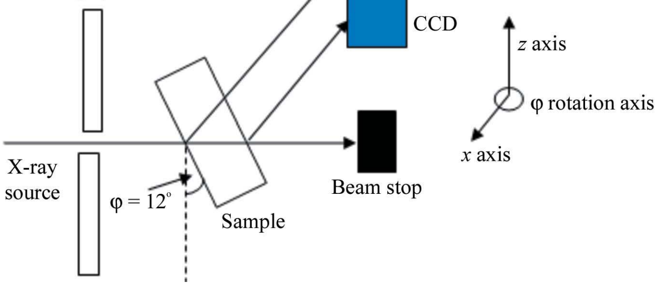

**Figure 1**
Schematic illustration of the experimental arrangement for ST topography. $\varphi$ rotation occurs around the $x$ axis. The sample is mounted so the features of interest are facing the CCD.

The CCD camera system, positioned 16 cm from the sample, comprises a pco.4000 14 bit cooled CCD camera system from PCO Imaging. The CCD has a resolution of 4008 × 2672 pixels with a pixel size of 9 × 9 μm. The CCD was run with 3.6× Rodenflex 'TV-Heliflex' magnification optics leading to an effective pixel size of 2.5 × 2.5 μm and utilized a scintillating screen 22 × 4 mm in size fabricated from a 300 μm-thick Ce-doped $\mathrm{Lu_3Al_5O_{12}}$ crystal polished on both sides to optical quality (Danilewsky *et al.*, 2008; Nagornaya *et al.*, 2005). The CCD was positioned to capture the $2\bar{2}0$ reflection. Utilizing the $z$ translation the sample was then stepped vertically in 15 μm steps resulting in a series of section topograph diffraction images being taken.

The resulting images were then normalized using a dark-field image to eliminate machine-induced artefacts. After normalization, the images were stacked together using *ImageJ* image-processing software (Abramoff *et al.*, 2004), the stack being the basis of the three-dimensional rendering of the image.

## 3. Three-dimensional rendering

While section topography does not directly allow for the generation of three-dimensional images, it does allow, under low-absorption conditions, for the reconstruction of the three-dimensional shape of the original object from the projection of the direct image. The method used in this paper is an application of the Fourier slice theorem to a Radon transform of the topographic images.

The Radon transform gives the projected intensity of the X-ray along the projection beam as a line integral. The slice theorem states that, given an infinite number of projections, the original object can be reconstructed by means of finding

**Figure 2**
3D-XRDI experimental setup. 'A' is the fast shutter, collimating the beam to 10 × 1 mm. 'B' is the final slit system to collimate the beam to 10 mm × 15 μm. 'C' is the sample holder containing a 200 mm wafer. 'D' is the CCD camera system.

the inverse Radon transform. Filtered back projection is used in the inverse transform process to eliminate the inherent instability of the Radon transform with respect to noise (Jähne, 2005). *ImageJ*, using Java3D, then renders the visual image using three-dimensional texture mapping and volume rendering as described by Levoy (1988),

The number of topographs obtained can be adjusted according to the size of the feature to be examined and is only dependent upon the beam time available to obtain the scans and the size of the storage media. The scans were obtained using a stepping algorithm that matched the slit size to the step size to ensure complete coverage of the feature. The scan-limiting factor is the acquisition time for each scan, which should be long enough to capture the information required but sufficiently short so as not to induce saturation in the final image. The image shown in Fig. 4 below shows a rendering of 45 individual ST topographs which required ~4 h to capture. The inclusion of the slit system 'B' shown in Fig. 2 provides higher resolution; as such, the acquisition time for each topograph has been reduced to <500 ms. With this, ~300 images can now be captured in the same time.

## 4. Results and discussion

Fig. 3 depicts a $0\bar{2}2$ reflection of three 600 mN indents. This transmission-mode X-ray diffraction image was captured on the CCD system. A series of time-stamped large-area $0\bar{2}2$ transmission topographs are shown for this sample, which has undergone *in situ* thermal annealing as described earlier (Wittge *et al.*, 2010).

We will now describe the use of 3D-XRDI techniques for the analysis of the structure of these loops.

A series of ST topographs were obtained by stepping horizontally across the line A–A′ shown in Fig. 3. Fig. 4 shows a single ST topograph where individual dislocation half-loops can be observed on the left-hand side of the image. The dislocation density on the right-hand side of the image is so great that the individual half-loops cannot be easily distinguished. The preferred glide plane for (100) silicon corresponds to the {111} series of glide planes (Vallino *et al.*, 2000) and is calculated out to 54.7° (Fig. 5). It can be seen from Fig. 4 that the loops are gliding from the sample surface at an angle of ~54°.

Once imported into the imaging software, both the contrast and the brightness of the stack were adjusted to maximize the image resolution. The three-dimensional project plug-in is then selected, and at this point the spacing between the image slices needs to be entered. The spacing size can be evaluated by

$$S = k/v, \tag{1}$$

where $S$ is the image spacing, $v$ is the resolution in µm pixel$^{-1}$ and $\kappa$ is the step size in µm (Fig. 6).

The resulting image is then rendered into three dimensions utilizing the three-dimensional viewer plug-in within *ImageJ* (Fig. 7).

Fig. 8 shows the final three-dimensional image rendered from a stack consisting of 45 individual ST topographs saved in a lossless format, TIFF in this case, giving a file size of 4.8 Mb.

It can be noted that the dislocation loops observed in Fig. 8 are easily identifiable. This image can be manipulated to

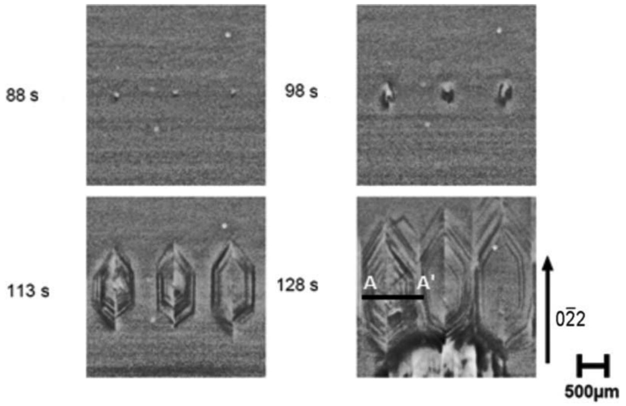

**Figure 3**
A series of time-stamped $0\bar{2}2$ large-area transmission topographs of three 600 mN indents captured during *in situ* heating of the sample. A–A′ indicates where the ST is positioned for Fig. 5.

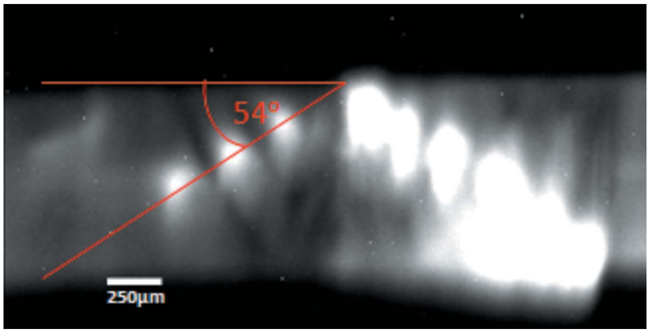

**Figure 4**
Illustration of the glide planes and dislocation loops shown in Fig. 3. Each dislocation half-loop is on a different slip plane, (111) and $(\overline{111})$.

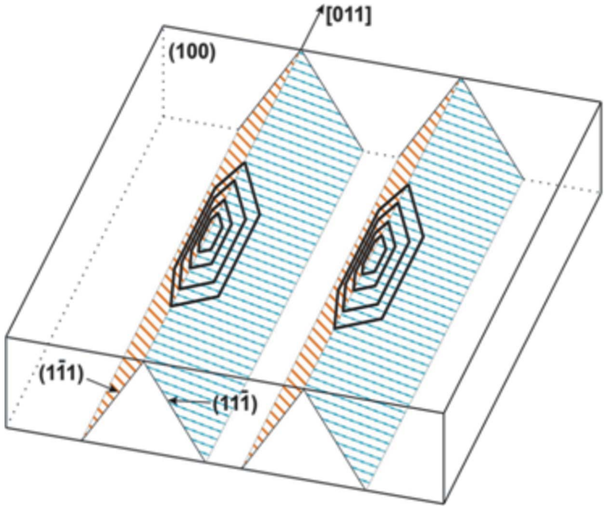

**Figure 5**
Single $0\bar{2}2$ ST topograph, taken at position A–A′ as indicated in Fig. 3. Dislocation loops are gliding at ~54° from the top surface.

provide different views of the area of interest, and it is also possible, though not shown here, to save the rotation of the image as a video (avi) file and to run the manipulation of the image in a movie-type format. The image also can be split by use of a segmentation line. An example, labelled B–B′, is shown in Fig. 8.

In this case, a segmentation line was drawn along the axis perpendicular to the propagation direction of the dislocation half-loop, and the image was split along this line. Rotation of the image (Fig. 9) demonstrates that the dislocation loops are gliding from the surface of the sample at an angle of ∼54°, agreeing with Fig. 4.

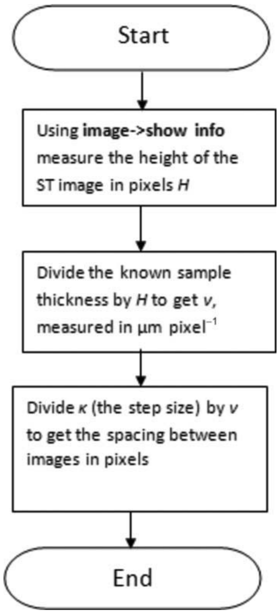

**Figure 6**
Flow chart showing the steps required to obtain the slice spacing in *ImageJ*.

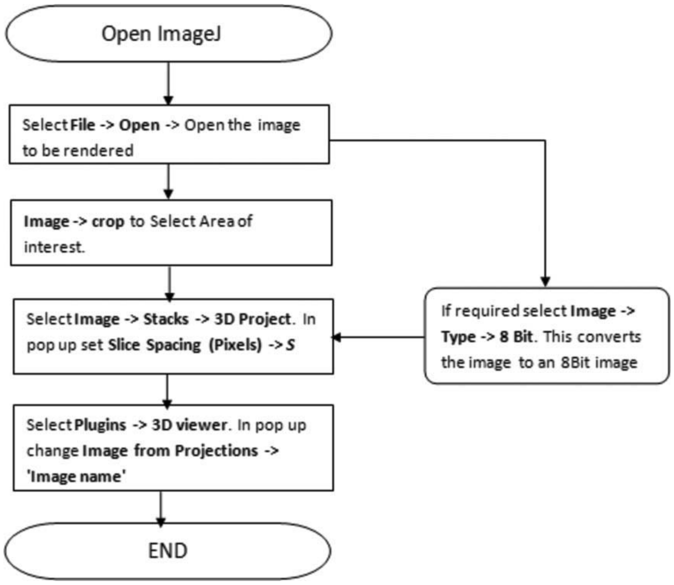

**Figure 7**
Flow chart showing the steps required to produce a 3D-XRDI image in *ImageJ*.

The rendered image can be processed using a $k$-means clustering algorithm of the type

$$J = \sum_{j=1}^{k}\sum_{i=1}^{n}\|x_i^{(j)} - c_j\|^2, \qquad (2)$$

where $k$ is the number of clusters, *i.e.* the number of segments that the image will be divided into, $n$ is the number of data points, and $\|x_i^{(j)} - c_j\|^2$ is the distance between a data point $x_i^{(j)}$ and the cluster centre $c_j$, so giving a graphical indication of the areas of greatest strain (MacKay, 2003).

Fig. 10 shows the result of running a $k$-means cluster algorithm performed on Fig. 6. Applied false colouring highlights the areas of maximum strain in teal and minimum strain-induced contrast in green.

Another example of this technique was applied to Fig. 11, a line of five indents created using a Vickers tip with a 2 N load. These samples were not annealed in order to observe the

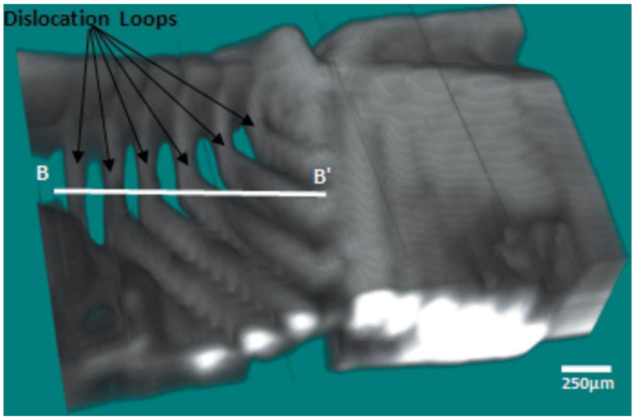

**Figure 8**
Three-dimensional rendering of the dislocation loops observed in Fig. 3. In the left-hand side of the image the dislocation density is so great it is impossible to distinguish individual dislocation half-loops.

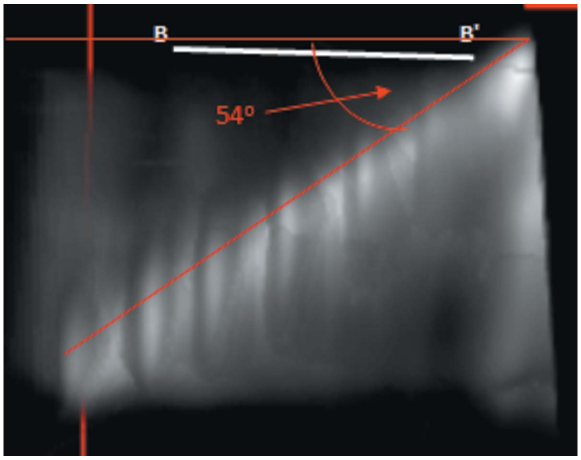

**Figure 9**
Segmented image of dislocation loops. The loops are gliding along the {111} plane system, *i.e.* ∼54°.

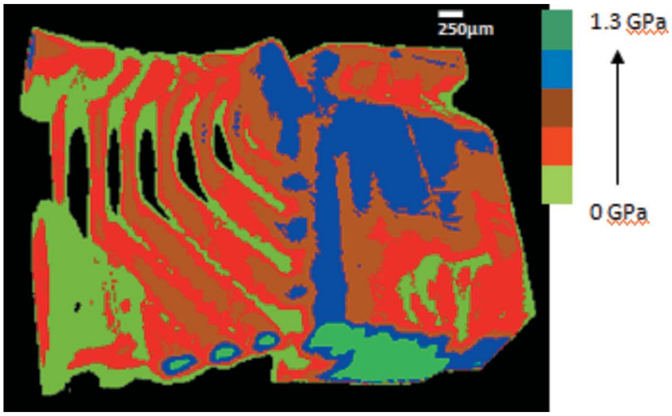

**Figure 10**
*k*-means cluster processing of a 3D-XRDI image of dislocation loops with false colour added to highlight areas of high strain-induced contrast.

**Figure 11**
Scanning electron microscope image of the five indents from the 20 × 20 mm silicon sample shown in Fig. 12.

unchanged three-dimensional strain distributions around the indents (Fig. 12).

False colouring shows the area of maximum strain in red.

In Fig. 13, a segmentation line, C–C′, is drawn through one of the indents and the image split along this line.

One of the advantages of using the ST technique is that it can reveal the location and depth of defects in the crystal (Authier *et al.*, 1996; Bowen & Tanner, 1998; McNally *et al.*, 2001; Tanner, 1989). This can be observed in Fig. 12 where the depth profile of the strain field is visible running into the bulk silicon. Measurement of the depth of the strain field indicates that it is similar in size to the width, agreeing with finite element simulation models presented in a previous paper (Allen *et al.*, 2010), and that it is of the order of ~150 µm.

## 5. Conclusion

An improved methodology is described which produces 3D-XRDI images that aid in the analysis of the three-dimensional strain fields within silicon. This method improves resolution with an effective pixel size of 2.5 × 2.5 µm, which can be used to observe the strain fields and dislocation structures of both wafer samples and complete 300 mm wafers. The use of open-source software provides a level of automation to both the capturing of the topographs and the rendering, allowing for the capture of section topographs and subsequent rendering of the topographs into three dimensions in ~2–3 h. Previous methods utilized either the taking of stereoscopic pairs of topographs or the rotation of the sample around its diffraction vector, essentially combining topography and tomography. The technique reported here simplifies the process by taking a series of section X-ray topographs using a *z*-translation movement of the goniometer combined with readily available open-source image-processing software to provide three-dimensional X-ray diffraction images. Images were obtained both from 20 × 20 mm silicon wafer samples and from full 200 mm silicon wafers that were nano-indented to introduce controlled strain. The processing software allowed for the production of a video (avi) file showing the rotation of the three-dimensional rendered diffraction images around any defined axis. The software also has the capability of splitting the image along a segmentation line and viewing the internal structures of the strain fields and dislocation structures.

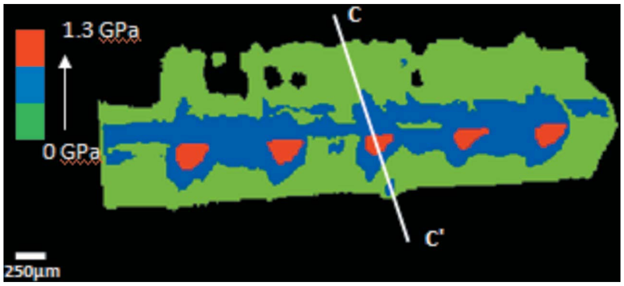

**Figure 12**
3D-XRDI rendering of a line of 2 N Vickers indents with segmentation line C–C′.

**Figure 13**
Segmentation of Fig. 8. Areas of highest strain are in red.

We would like to thank P. Vagovič and H. Shade at ANKA for their technical support and J. Garagorri and M. R. Elizalde for the indentation provision. Financial support by EU-FP7 project No. 216382 SIDAM is gratefully acknowledged. This work was part-funded by the Irish Higher Education Authority PRTLI 'INSPIRE' project and also supported by the European Community–Research Infrastructure Action under the FP7 'Structuring the European Research Area' programme.

## References

Abramoff, M. D., Magalhaes, P. J. & Ram, S. J. (2004). *Biophoton. Int.* **11**(7), 36–43.

Allen, D., Wittge, J., Zlotos, A., Gorostegui-Colinas, E., Garagorri, J., McNally, P. J., Danilewsky, A. N. & Elizalde, M. R. (2010). *Nucl. Instrum. Methods Phys. Res. Sect. B*, **268**, 383–387.

Authier, A. (2004). *Dynamical Theory of X-ray Diffraction*, 1st ed. Oxford University Press.

Authier, A., Lagomarsino, S. & Tanner, B. K. (1996). Editors. *X-ray and Neutron Dynamical Diffraction Theory and Applications.* New York: Plenum Press.

Bowen, D. K. & Tanner, B. K. (1998). *High Resolution X-ray Diffractometry and Topography*, 1st ed. London: Taylor and Francis.

Cholewa, M. & Rack, A. (2007). *ANKA Instrumentation Book*, http://ankaweb.fzk.de/_file/extras/extras_download_3.pdf.

Danilewsky, A. N., Rack, A., Wittge, J., Weitkamp, T., Simon, R., Riesemeier, H. & Baumbach, T. (2008). *Nucl. Instrum. Methods Phys. Res. Sect. B*, **266**, 2035–2040.

Danilewsky, A. N., Simon, R., Fauler, A., Fiederle, M. & Benz, K. W. (2003). *Nucl. Instrum. Methods Phys. Res. Sect. B*, **199**, 71–74.

Danilewsky, A. N., Wittge, J., Hess, A., Cröll, A., Allen, D., McNally, P. J., Vagovič, P., Cecilia, A., Li, Z., Baumbach, T., Gorostegui-Colinas, E. & Elizalde, B. R. (2010). *Nucl. Instrum. Methods Phys. Res. Sect. B*, **268**, 399–402.

Guinier, A. & Tennevin, J. (1949). *Acta Cryst.* **2**, 133–138.

Hart, M. (1975). *J. Appl. Cryst.* **8**, 436–444.

Jähne, B. (2005). *Digital Image Processing: Concepts, Algorithms and Scientific Applications*, 6th ed. Berlin: Springer.

Kajiwara, K., Kawado, S., Iida, S., Suzuki, Y. & Chikaura, Y. (2007). *Phys. Status Solidi*, **204**, 2682–2687.

Kawado, S. & Aoyama, J. (1979). *Appl. Phys. Lett.* **34**, 428–429.

Kawado, S., Taishi, T., Iida, S., Suzuki, Y., Chikaura, Y. & Kajiwara, K. (2004). *J. Synchrotron Rad.* **11**, 304–308.

Kawado, S., Taishi, T., Iida, S., Suzuki, Y., Chikaura, Y. & Kajiwara, K. (2005). *J. Phys. D*, **38**, A17–A22.

Kvardakov, V. V., Podurets, K. M., Schetinkin, S. A., Baruchel, J., Härtwig, J. & Schlenker, M. (2007). *Nucl. Instrum. Methods Phys. Res. Sect. A*, **575**, 140–143.

Lang, A. R. (1959*a*). *Acta Cryst.* **12**, 249–250.

Lang, A. R. (1959*b*). *J. Appl. Phys.* **30**, 1748–1755.

Levoy, M. (1988). *IEEE Comput. Graph. Appl.* **8**(3), 29–37.

Ludwig, W., Cloetens, P., Härtwig, J., Baruchel, J., Hamelin, B. & Bastie, P. (2001). *J. Appl. Cryst.* **34**, 602–607.

MacKay, D. (2003). *Information Theory, Inference, and Learning Algorithms*, edited by D. MacKay, pp. 284–292. Cambridge University Press.

McNally, P. J., Tuomi, T., Lowney, D., Jacobs, K., Danilewsky, A. N., O'Hare, M. & Considine, L. (2001). *Phys. Status Solidi*, **185**, 373–382.

Mukaide, T., Kajiwara, K., Noma, T. & Takada, K. (2006). *J. Synchrotron Rad.* **13**, 484–488.

Nagornaya, L., Onyshchenko, G., Pirogov, E., Starzhinskiy, N., Tupitsyna, I., Ryzhikov, V., Galich, Y., Vostretsov, Y., Galkin, S. & Voronkin, E. (2005). *Nucl. Instrum. Methods Phys. Res. Sect. A*, **537**, 163–167.

Rack, A. *et al.* (2009). *Nucl. Instrum. Methods Phys. Res. Sect. B*, **267**, 1978–1988.

Simon, R. & Danilewsky, A. N. (2003). *Nucl. Instrum. Methods Phys. Res. Sect. B*, **199**, 550–553.

Tanner, B. K. (1989). *J. Electrochem. Soc.* **136**, 3438–3443.

Tuomi, T., Naukkarinen, K. & Rabe, P. (1974). *Phys. Status Solidi*, **25**, 93–106.

Vallino, F., Jacques, A. & George, A. (2000). *Phys. Status Solidi*, **222**, 51–62.

Wittge, J., Danilewsky, A. N., Allen, D., McNally, P. J., Li, Z., Baumbach, T., Gorostegui-Colinas, E., Garagorri, J., Elizalde, M. R., Jacques, D., Fossati, M. C., Bowen, D. K., Tanner, B. K. (2010). *J. Appl. Cryst.* **43**, 1036–1039.